Article ID: 1006-8775(2019) 02-0227-18

A COMPARISON OF THE BLENDING AND CONSTRAINING METHODS TO INTRODUCE LARGE–SCALE INFORMATION INTO GRAPES MESOSCALE ANALYSIS

YANG Mei-jin (杨枚锦)[1], GONG Jian-dong (龚建东)[2, 3], WANG Rui-chun (王瑞春)[2, 3],
ZHUANG Zhao-rong (庄照荣)[2, 3], XU Zhi-fang (徐枝芳)[2, 3]
(1. Nanjing University of Information Science and Technology, Nanjing 210044 China; 2. Center of Numerical Weather Predication, China Meteorological Administration, Beijing 100081 China;
3. National Meteorological Center, Beijing 100081 China)

Abstract: To solve the problem of mesoscale analysis error accumulation after a period of continuous cycle data assimilation (CCDA), a blending method and a constraining method are compared to introduce global analysis information into the Global/Regional Assimilation and Prediction Enhanced System mesoscale three-dimensional variational data assimilation system (GRAPES-Meso 3DVar). Based on a spatial filter used to obtain a blended analysis, the blending method is weighted toward the T639 global analysis for scales larger than the cutoff wavelength of 1,200 km and toward the GRAPES mesoscale analysis for wavelengths below that. The constraining method considers the T639 global analysis data as an extra source of information to be added in the 3DVar cost function. The cloud-resolving GRAPES-Meso system (3 km resolution) with a 3 h analysis cycle update is chosen, and forecast experiments on an extreme precipitation event over the eastern part of China are presented. The comparison shows that the inclusion of large-scale information with both methods has a positive impact on the regional model, in which the 3 h background forecasts are slightly closer to the radiosonde observations. The results also show that both methods are effective in improving large-scale analysis while reserving the well-featured mesoscale information, leading to an enhancement in the balance and accuracy of the analysis. Subjective verification reveals that the introduction of large-scale information has a visible beneficial impact on the forecast of precipitation location and intensity. The methodologies and experiences presented in this paper could serve as a reference for ongoing efforts toward the development of multi-scale analysis in GRAPES-Meso.

Key words: numerical prediction; data assimilation; blending and constraining method; large-scale information; GRAPES mesoscale analysis
CLC number: P435 **Document code:** A
doi: 10.16555/j.1006-8775.2019.02.009

1 INTRODUCTION

The simultaneous assimilation of broadly distributed observations to generate a mesoscale analysis that reflects many scales of atmospheric motion is desired, and a multi-scale data assimilation method is needed. However, a higher resolution cloud-resolving limited area model (LAM) provides a better representation of mesoscale to small-scale phenomena, whereas larger scales are not well specified in an LAM analysis compared with the hosting global model analysis (Berre[1]). For mesoscale continuous cycle data assimilation (CCDA), there are several challenges for large-scale analysis. The first challenge is the existence of lateral boundaries. Since observations outside the mesoscale model boundaries do not influence the analysis within the model domain, the quality of analysis near the model's lateral boundaries can be degraded (Hsiao et al.[2]). A negative impact might also arise if the analysis of a large-scale feature requires information from a large-scale observational network lying partly outside the domain. Another challenge is the lack of observations over the domain. One important source of data for global analysis is the information from satellite radiance assimilation, which can be quite important in data-sparse regions, but this information is generally not available in mesoscale analysis. Regional density observation networks, such as weather radar, automated weather stations, wind profilers, and GPS/PW, may not have good spatial coverage. Romine et al. found that a long period of continuous cycling revealed significant biases in the analyses, and the subsequent cloud-resolving forecasts had limited abilities, which were noticeably inferior to forecasts initialized from the global forecast system analysis[3]. The authors also found that the analysis bias was influenced not only by

Received 2018-01-22; **Revised** 2019-02-02; **Accepted** 2019-05-15
Foundation item: National Key R&D Program of China (2018YFC1506705); National Natural Science Foundation of China (41705085)
Biography: YANG Mei-jin, Ph.D., primarily undertaking research on the assimilation of atmospheric data.
Corresponding author: GONG Jian-dong, e-mail: gongjd@cma.gov.cn

systematic error caused mainly by model physics but also by bias differences between observation platforms. With a lack of sufficient observations to correct the background error, systematic biases can accumulate in the initial conditions after a period of continuously cycled analysis. Moreover, by using background error covariance models to represent mesoscale dynamic characteristics (Siroka et al.[4]), and by using dense observation networks, such as weather radar observations or radar retrieved products (Zhang et al.[5]), mesoscale data assimilation systems are designed for mesoscale and smaller-scale applications. Berre[1] reported that background error sampling for scales larger than one-quarter of the longest wave over the LAM domain size becomes questionable. Berre et al. also showed that the analysis process uses the observations to reduce the amplitude of the large-scale portion of the background errors, resulting in the distortion of large-scale information after the mesoscale analysis[6].

Mesoscale analysis and forecasts also suffer from the lateral boundary conditions (LBCs) problem. LBCs are generally treated in a manner that is not well posed or physically sound. The Davies relaxation method (Davies[7]) is adopted in many LAMs, but since they are not well posed, atmospheric phenomena may be poorly propagated through the LAM boundaries. The LBC formulation errors can have an adverse effect on the large-scale three-dimensional shape and propagation properties of large-scale baroclinic waves in the atmosphere (Guidard and Fischer [8]). During mesoscale CCDA, the continuous refreshing of the LBCs from a global boundary condition would not be sufficient for the LAM system to maintain the large-scale structures analyzed by the global model (Sadiki et al. [9]). For non-hydrostatic cloud-resolving models with CCDA, the smaller size of the domain means that such systems can be highly dependent on lateral boundary coupling and large-scale relaxation formulations[8].

Several methods have been proposed to utilize global model analysis to improve the initial conditions of the LAMs and compensate for the lack of information on larger scales. Brozkova et al. introduced the digital filter blending method, which is applied in spectral space with a low-pass digital filter to incrementally blend a large-scale analysis with the small scales of LAM [10]. Digital filter blending is an implicit blending method for the spectral transition zone, which is implicitly defined by using an incremental digital filter initialization technique (Lynch et al. [11]). Siroka et al. proposed combining digital filter blending with the 3DVar method, with digital filter blending applied either before or after the 3DVar method[4]. The combination of the two methods leads to an improved LAM assimilation system with a forcing toward the global hosting system. Guidard et al. showed the positive impact of this method on a 24 h assimilation period as well as the improvement of the forecast accuracy in subsequent model forecasts[12].

Another approach to improve the quality of the initial conditions is the employment of an explicit blending method, in which the spectral transition zone is explicitly defined by using a predefined low-pass spatial filter. Yang used an incremental spatial filter to blend the large-scale analysis from the European Centre for Medium-Range Weather Forecasts (ECMWF) with the small-scale fields from the High Resolution Limited Area Model (HIRLAM)[13]. Wang et al. found the results of blending-based schemes to be promising with respect to simple 3DVar alone[14]. Hsiao et al. utilized the same blending method to merge the NCEP global analysis with the regional analysis from the WRF 3DVar system for the purpose of initializing the typhoon WRF model[15]. They found that the blended analysis takes advantage of both global analysis and mesoscale analysis.

Since digital filter blending has few relationship with statistical concepts such as maximum likelihood and error representation, Guidard and Fischer proposed the use of the global analysis as an extra source of information to be added to the cost function of LAM 3DVar[8]. An extra penalty term in the cost function would measure the weighted distance between the global analysis and LAM background. The global analysis is truncated at a low wavenumber to ensure that only large scales are penalized in the analysis. Dahlgren and Gustafsson used the same approach[16] but assimilating only the vorticity field from the global analysis and using global analysis error covariances that were not simplified by a diagonal matrix as in Guidard and Fischer[8]. Vendrasco et al. added a large-scale analysis constraint to the cost function[17]. They also found that this constraint is able to guide the assimilation process in such a way that the final result still maintains the large-scale pattern while adding the convective characteristics where radar data are available.

The non-hydrostatic GRAPES model and data assimilation system have been operationally utilized since 2006. The latest version of GRAPES-Meso 4.0 began operation in 2017. This model adopts the 3Dvar analysis technique, with 10 kilometers horizontal resolution and 50 vertical levels. The cloud-resolving version of GRAPES-Meso 4.0 with a 3 kilometer resolution has been running in real time in eastern China since 2015. The initial condition comes from T639 analysis downscaling. The Davies relaxation[7] method is adopted for the LBCs, which are not well posed for the model. Huang et al. found that the weaknesses of GRAPES-Meso include over-prediction of precipitation, large 2 m temperature forecast errors, etc[18]. Wang et al. found that 8 times per day, the 3 h forecasts of the 2 m temperature from the GRAPES-Meso CCDA are lower, on average, than the observation on the western Sichuan Plateau in eastern Tibet, the Yungui Plateau and the Wuyi Mountains but are higher than the observations in North China[19]. Xu and Wang used the quantitative precipitation forecast (QPF) of GRAPES-Meso 4.0 to evaluate the precipitation accumulation, frequency, intensity and diurnal cycle[20]. They found that the predicted heavy

precipitation intensity is stronger than the observations for the diurnal cycle of hourly precipitation and that the precipitation frequency has a weaker peak in the afternoon. Huang et al. found that the observations used in GRAPES-Meso 3Dvar are less preferable because satellite radiance assimilation may be quite indispensable over the marine areas in the regional model domain[18]. To reduce the error of the GRAPES-Meso initial conditions, we adopt the blending method from Yang [13] and the constraining method from Guidard and Fischer[8] to merge the large-scale analysis information from the China Meteorological Administration T639 L60 global spectral operational forecast system (hereafter called T639) with the mesoscale analysis data from GRAPES-Meso 3Dvar. Comparative studies of the blending and constraining method are undertaken to find a suitable method for the GRAPES-Meso CCDA.

The paper is organized as follows. The blending method and the constraining method are described in detail in Section 2. Section 3 describes the model configuration and experimental setup. The experimental results as well as impacts on the analysis and forecast are given in Sections 4 and 5, respectively. The conclusions are given in Section 6.

2 METHODOLOGY

2.1 *Blending method*

An explicit spatial blending method proposed by Yang[13] is adopted in this study. This blending method utilizes an incremental spatial filter to combine the large-scale analysis from T639 and the mesoscale analysis from GRAPES-Meso 3Dvar. The spectral transition zone is explicitly defined by using a predefined low-pass Raymond sixth-order tangent implicit filter (Raymond et al.[21]) with a fixed cutoff wavelength. The formula for the blending procedure can be denoted as follows:

$$X^{\mathrm{a}}_{\mathrm{bld}}(l)=X^{\mathrm{a}}_{\mathrm{meso}}(l)+\alpha(l)[X^{\mathrm{a}}_{\mathrm{glb}}(l)-X^{\mathrm{a}}_{\mathrm{meso}}(l)] \quad (1)$$

where $X^{\mathrm{a}}_{\mathrm{meso}}(l)$ is the GRAPES-Meso 3Dvar analysis field, $X^{\mathrm{a}}_{\mathrm{glb}}(l)$ is the T639 global analysis field, and $X^{\mathrm{a}}_{\mathrm{bld}}(l)$ is the blended mesoscale analysis field. The amplitude response function of the Raymond sixth-order tangent implicit filter to wavelength l is expressed as follows:

$$\alpha(l)=\left[1+\varepsilon\tan^{6}\left(\frac{\pi\delta x}{l}\right)\right]^{-1} \quad (2)$$

$$\varepsilon=\tan^{-6}\left(\frac{\pi\delta x}{l_c}\right) \quad (3)$$

where l is the wavelength in kilometers and ε is a filter parameter related to GRAPES-Meso grid spacing δx and cutoff wavelength l_c. From Equations (2) and (3), the power of the filter is 0.5 when $l=l_c$, which means that an identical weight will be given to GRAPES-Meso mesoscale analysis and T639 global analysis. The larger weight will be given to T639 global analysis for scales greater than the cutoff wavelength, and wavelengths below that will be assigned to GRAPES mesoscale analysis. The cutoff wavelength scale is a key parameter for the spatial blending method. Hsiao et al. found that the 1,200 km cutoff wavelength is a good choice to separate small-scale circulation patterns from the environmental flow when a vortex relocation scheme for tropical cyclone initialization is applied in the WRF model[2]. In the present study, we tested two cutoff wavelengths of 600 and 1,200 km, and we found that the cutoff wavelength of 1,200 km is better than 600 km for almost all precipitation thresholds, especially for the moderate precipitation threshold of 10 mm/D and the large precipitation threshold of 25 mm/D. Considering the findings of Hsiao et al.[2] and our test results, we choose the cutoff wavelength to be 1,200 km for all variables on all model levels(Fig. 1), which is rather imprecise without the consideration of spectral distribution for different variables on different model levels(Zhang et al.[22]). Fig. 1 also shows that there is almost no global information from T639 for wavelengths shorter than 600 km.

In practice, the blending procedure consists of several consecutive steps: 1) interpolating T639 global analysis fields with 30 km resolution into GRAPES-Meso model fields with 3 km resolution by using GRAPES Standard Interpolation software and then calculating the analysis departure between the global analysis and the GRAPES-Meso 3Dvar mesoscale analysis; 2) using the spatial to spectral space transform tool to convert the model fields of analysis departure to the spectral space; the two-dimensional discrete cosine transform (2D-DCT) method (Denis et al.[23]; Zheng et al.[24]) is utilized for the transform; 3) applying the Raymond sixth-order tangent implicit filter to the analysis departure in the spectral space, where the blending spectral transition zone is explicitly defined by the cutoff wavelength; 4) using the 2D-DCT method again but for the spectral to spatial space inverse transform to obtain the model grid field; and 5) adding the filtered analysis departure to the GRAPES-Meso 3Dvar analysis to obtain a blended mesoscale analysis field.

2.2 *Constraining method*

In the GRAPES-Meso 3DVar analysis formulation, the cost function is defined to measure the distance between the background state x_b and the mesoscale analysis x_a and between the observations y_o and x_a. To consider the T639 global analysis x_k as an extra source of information, in this study, the constraining method proposed by Guidard and Fischer[8] is adopted. A penalty term is added to the cost function of the 3Dvar data assimilation system. We also adopt similar simplifications for the formulation, as suggested by Guidard and Fischer[8], which assumes that the errors of large-scale information from the T639 analysis are uncorrelated with either the background state or observations; moreover, the global analysis error covariance is treated as a diagonal matrix. Vendrasco et al. added a large-scale analysis

constraint to the cost function of a radar 3Dvar data assimilation system[17]. They also assumed the large-scale analysis error covariance matrix for wind, temperature, and humidity to be an uncorrelated diagonal matrix with constant errors for each variable. The cost function with the global analysis constraint term J_k can be rewritten as follows.

$$J(x_a)=J_b(x_a)+J_o(x_a)+J_k(x_a)=\frac{1}{2}(x_a-x_b)^T B^{-1}(x_a-x_b)+\frac{1}{2}(\mathrm{H}_o(x_a)-y_o)^T R^{-1}(\mathrm{H}_o(x_a)-y_o)+\frac{1}{2}(\mathrm{H}_k(x_a)-x_k)^T B_k^{-1}(\mathrm{H}_k(x_a)-x_k) \quad (4)$$

where matrix B is the background error covariance, matrix R is the observation error covariance and matrix B_k is global analysis error covariance. $\mathrm{H}_o(\cdot)$ is the nonlinear observation operator, which maps the mesoscale analysis to the observation space, and H_k is the linear interpolation operator, which maps the mesoscale analysis with higher resolution to the global analysis with coarse resolution. The innovation vector is defined as $d_o=\mathrm{H}_o x_b-y_o$. For comparison, the global analysis departure is also defined as $d_k=\mathrm{H}_k x_b-x_k$. Before the global analysis departure is calculated, the T639 global analysis fields are truncated at wavelengths larger than 1,200 km to ensure that only large scales are penalized in the analysis. x_k is then thinned to a coarse resolution to avoid having the dominance of the J_k term in the cost function. The thinning experiment shows that a 300 kilometer resolution is suitable. The thinned data are then treated as one type of "observation" to calculate the global analysis departure. With linear observation operator H_o, Equation (4) can be rewritten as an analysis increment format:

$$J(\delta x_a)=\frac{1}{2}\delta x_a^T B^{-1}\delta x_a+\frac{1}{2}(\mathrm{H}_o\delta x_a+d_o)^T R^{-1}(\mathrm{H}_o\delta x_a+d_o)+\frac{1}{2}(\mathrm{H}_k\delta x_a+d_k)^T B_k^{-1}(\mathrm{H}_k\delta x_a+d_k) \quad (5)$$

To reduce the condition number and to accelerate the minimization algorithm, the preconditioning of the background cost function is implemented by a control variable transform in GRAPES-Meso 3Dvar. The control variable w to mesoscale analysis state variables is defined as $\delta x_a = U_{\mathrm{W}}$, where U is defined as $B=UU^T$ (Derber and Bouttier [25]). The cost function with respect to the control variable is as follows:

$$J(\mathrm{w})=\frac{1}{2}\mathrm{w}^T\mathrm{w}+\frac{1}{2}(\mathrm{H}_o\mathrm{U}\mathrm{w}+\mathrm{d}_o)^T R^{-1}(\mathrm{H}_o\mathrm{U}\mathrm{w}+\mathrm{d}_o)+\frac{1}{2}(\mathrm{H}_k\mathrm{U}\mathrm{w}+\mathrm{d}_k)^T B_k^{-1}(\mathrm{H}_k\mathrm{U}\mathrm{w}+\mathrm{d}_k) \quad (6)$$

With this definition, the extra penalty term for large-scale information is conveniently added to the cost function of GRAPES-Meso 3Dvar. Global analysis error covariance matrix B_k is assumed to be a diagonal matrix, and the error estimation is essential for using global analysis information.

In an operational setting, the background error covariances for T639 3Dvar are estimated from forecast samples of 24 h and 48 h differences verified at the same time by using the National Meteorological Center (NMC) method (Parrish and Derber[26]). There is no estimation of analysis error covariances in an operational setting. Derber and Bouttier[25] estimated the 6 h forecast error variance by inflating the analysis error variances using the error growth model of savijarvi[27] for the evolution of standard errors. With this error growth model, the analysis error variances would increase by approximately 1.05- to 1.1-fold in 6 h or the background error variances are approximately 1.05 to 1.1 times larger than the analysis error variances. In this study, we simply multiply 0.9 by the background error variances to obtain the analysis error variances.

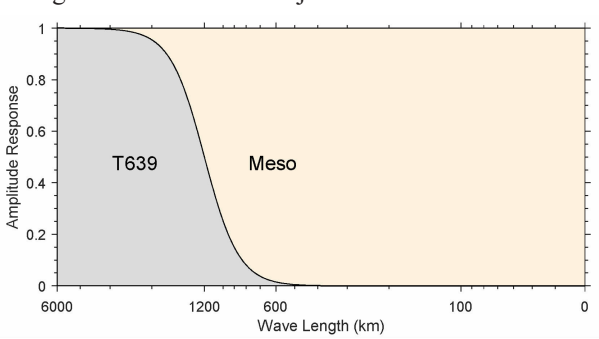

Figure 1. Amplitude responses for the Raymond filter as a function of wavelength with a cutoff of 1,200 km. The Global and Meso models are demonstrated as T639 global analysis and GRAPES-Meso analysis, respectively.

3 CASE STUDY AND EXPERIMENTAL SETTING

3.1 *Case study*

An extremely severe precipitation event occurred in north China on 19-20 July 2016, which was triggered by an eastward-moving circulation of a South Asia high together with the northwestward-moving Western Pacific subtropical high and the low vortex (LV) in the westerlies, which was born and developed in the mid-high latitudes. The characterization of this event is large and persistent, with strong locally intense convective precipitation and orographic precipitation. The abnormal development of the Huanghuai (a basin between Yellow River and Huaihe River) cyclone, northwest and southeast low-level jets, and the abnormally abundant moisture together indicated that dynamic lifting and moisture conditions would greatly facilitate this severe precipitation process (Fu et al.[28]). From the early morning (local time, 0000 UTC) to midday on 19 July, heavy precipitation was orographic, and convective precipitation was caused by the easterly winds ahead of the trough.

From the night of local time (1800 UTC) of 19 July to the daytime of 20 July, the second part was produced by spiral rain bands on the north side of the Huanghuai cyclone from nighttime local time (1800 UTC) on 19 July to the daytime on 20 July. Fig. 2 shows the 24 h accumulative precipitation observations of 2,500 stations in China during 0000 UTC on 19-20 July, from which we can conclude that at 0000 UTC 19-20 July, most of the heavy precipitation over 50 mm was centered in southern Beijing and Hebei Province, the central part of Hubei Province, and the border between Chongqing and Hunan Province.

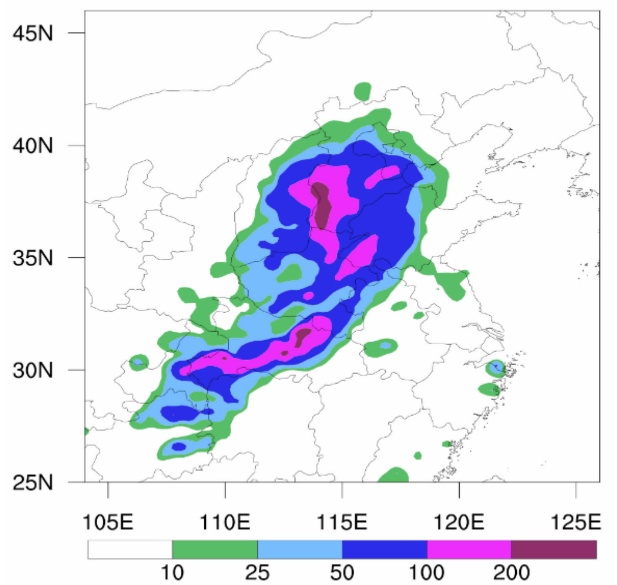

Figure 2. 24 h accumulative precipitation at 0000 UTC 19-20 July.

For the mesoscale characteristics of this heavy precipitation event, according to the evolution of composite radar reflectivity, it is clear that at 1600 UTC on 18 July, randomly distributed convective cells developed from the north of Henan Province to the south of Hebei Province along the eastern foothills of the Taihang Mountains (figure not shown). The cells were northward moving when convection systems were impacted by the southerly winds before the upper-level trough. The first belt-shaped arrangement of the convective cells along the south-north direction was formed at 2000 UTC on 18 July (hereafter called the first convection system) and remained stationary. At the same time, another well-organized belt-shaped convection system along the southwest-northeast direction, which is also near the upper-level trough, was located at the border between Shaanxi and Shanxi Provinces (hereafter called the second convection system). When the upper-level trough developed and moved eastward, the second convection system also moved eastward. At 0000 UTC on 19 July, the second convection system was located along the central part of Shaanxi Province to the central and western part of Shanxi Province (Fig. 10). The second convection system began to merge with the first convection system to form a new belt-shaped convection system at 0600 UTC on 19 July. This new system remained stationary until 1200 UTC on 19 July. At the same time, an upper-level low vortex circulation system (LVCS) was formed, and the center of the low vortex was located in central and northern Henan Province at 1200 UTC on 19 July. This system moved slowly northward and was located in the south of Hebei Province at 0000 UTC on 20 July (Fig. 11). In this study, our interests are mainly focused on the capability of CCDA mesoscale analysis and subsequent model forecasts for this heavy precipitation event at 0000 UTC on 19-20 July.

3.2 *Model configuration*

The cloud-resolving version of GRAPES-Meso 4.2 adopts a regular latitude-longitude grid with 0.03° horizontal resolution and 50 levels in the vertical direction, with a model top of approximately 10 hPa. The model state variables include zonal wind u and meridional wind v, potential temperature θ, Exner pressure π, specific humidity q and other hydrometeors. The default physical process parameterization schemes include the WSM6 microphysical process parameterization scheme, the RRTM longwave radiation scheme, the Dudhia shortwave radiation scheme, the Monin-Obukhov planetary boundary layer scheme, the Noah land surface process scheme and the MRF planetary boundary layer scheme. No deep cumulus convection scheme is used in the experiments. The model domain in this study is set to (17°-50°N, 102°-135°E) (Fig. 3), which is similar to the model configuration of the real time running system. The northwestern model domain is occupied by mountains and highlands, and more than one-third of the model domain is covered by the Western Pacific Ocean. The GRAPES mesoscale 3DVAR data assimilation system has the same horizontal and vertical resolutions as the model configuration. The 3DVAR analysis state variables include u, v, π, and the humidity variable (relative humidity or specific humidity) (Ma et al. [29]). The potential temperature θ is deduced by the hydrostatic relationship between π and θ. The background error covariance is estimated using the NMC method, and a Gaussian regression function is employed to calculate the background error horizontal correlation structure. Xue et al. [30, 31] attempted to construct a reasonable background error covariance for multi-scale data assimilation, but this technique is not yet available in GRAPES-Meso 4.0. The observation data used in 3Dvar include radiosonde, Airep, Synop, ships and buoys, atmospheric motion vectors (AMVs), VAD wind retrieval from radar radial wind, wind profiler, and ground-based GPS/PW data. The observations are scarce in mountainous areas and especially over the ocean. Table 1 lists the observation stations or data counts used in the experiments, and Fig. 4 gives the radiosonde location in the model domain. The 3 h incremental digital filter is adopted after the 3DVar analysis to obtain a dynamic balanced initial field.

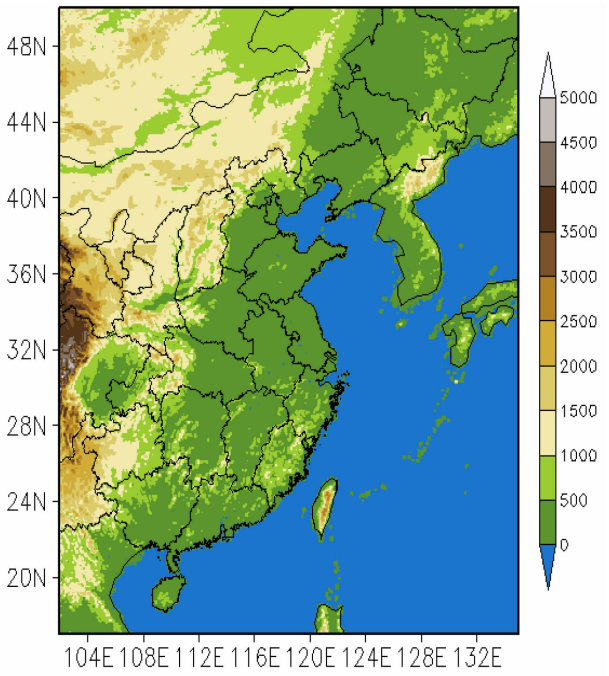

Figure 3. The model domain in this study is set to 17°-50°N, 102°-126°E.

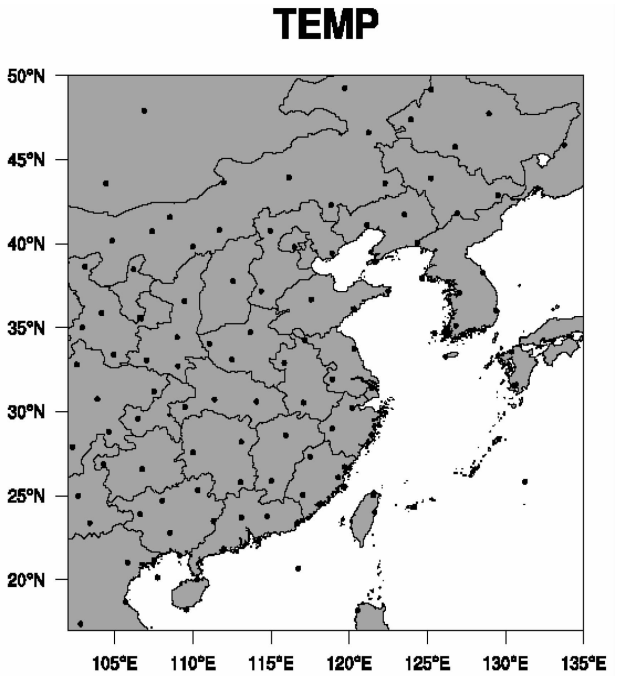

Figure 4. The distribution of radiosonde observations. There are a few radiosondes and other conventional observations over marine areas.

The hydrometeor variables of GRAPES-Meso 4.2 are not analyzed by 3DVar but are initialized by the three-dimensional cloud analysis scheme (Zhu et al.[32]). The data source ranges from Doppler weather radar three-dimensional mosaic reflectivity data to geostationary meteorological satellite data and surface observations. The nudging technique is employed for the cloud analysis, and the variables included are humidity, cloud water, cloud ice, rain, snow, graupel and temperature. The cloud analysis scheme is a convenient way to use weather radar reflectivity information in the mesoscale system. Compared with the global model analysis, the observations only used by mesoscale analysis and cloud analysis include relative humidity data from Synop; wind data from ships, radar VAD and wind profiler, and ground-based GPS/PW data; radar reflectivity data from 68 stations; total cloud cover data; and cloud top brightness temperature data from the Fengyun geostationary satellite. If the cloud analysis scheme is switched off, the hydrometeor variables are spun up by the microphysics process parameterization scheme during model integration.

Table 1. Observations used in 3DVar at 0000 UTC on 19 July.

Observation Type	Number of stations/data counts used in 3DVar
Radiosonde	135 stations (u, v, T or P, and RH)
Airep	3,974 data counts (u, v, T)
Synop	2,240/901 data counts (Ps/RH)
Ships and Buoys	45 data counts (u, v and Ps)
AMVs	249 data count (u, v)
Radar VAD	68 stations (465 data counts) (u, v)
Wind Profiler	93 stations (2175 data counts) (u, v)
GPS/PW	584 stations (PW)

T639 global analysis downscaling is used as the background for cold starting of the CCDA. The LBCs are also provided by the T639 in 3 h intervals. The ECMWF ERA-interim reanalysis data set (hereafter called ERA data) at 0.5° resolution is interpolated to the grid points of GRAPES-Meso and serves as the real atmospheric state for large-scale patterns to verify the analyses of the experiments.

3.3 *Experimental design*

To reduce the error of the GRAPES-Meso initial conditions after a continuously cycled analysis and to explore the merits of the blending and constraining

method to merge the large-scale information from T639 analysis with the mesoscale analysis from GRAPES-Meso 3Dvar, several experiments are designed in this study. The control run is based on the traditional CCDA procedure, and the impact of T639 on the mesoscale analysis is determined according to the LBCs. The 24 h period CCDA with a 3 h updated analysis interval is used to obtain the initial condition, and then a 24 h forecast is performed. The explicit spatial blending on model surface (ESBM) experiment is based on the control run, but after GRAPES-Meso 3Dvar is completed and the mesoscale analysis field is obtained, the blending procedure based on Equation (1) is used to derive a blended analysis field. Instead of the original 3Dvar analysis field, the ESBM experiment utilizes the blended analysis field as the initial condition for next 3 h forecast to produce the background. The constraining experiment (JK) is also based on the control run. To compare the impact of the three-dimensional cloud analysis on the CCDA and forecast, an experiment with three-dimensional cloud analysis based on experiment JK (JKCA) is performed. Additionally, a global analysis downscaling experiment (GADN) that interpolates T639 global analysis to the GRAPES-Meso model as the initial condition is added. The experimental settings are listed in Table 2. In this paper, the CCDA procedure runs from 0000 UTC on 18 July to 0000 UTC on 19 July to obtain the final analysis field for experiments CNTL, ESBM, JK and JKCA. The analysis time of the GADN experiment is also set at 0000 UTC on 19 July, after which a 24 h forecast is performed for all experiments.

Table 2. Experimental setting.

Expt	Experimental setting
CNTL	3DVar with the cost function $J_b + J_o$.
ESBM	Explicit spatial blending on model level blended variable for u, v, π and q.
JK	3DVar with the cost function $J_b + J_o + J_k$, constrained u, v, T or p in J_k.
JKCA	Same as experiment JK, with three-dimensional cloud analysis.
GADN	Global analysis downscaling.

4 IMPACT ON ANALYSIS

4.1 *Mesoscale analysis difference*

The bias and root-mean-square error (RMSE) of the radiosonde innovation and residual are estimated first. The innovation calculated by radiosonde observation minus background field (O-B) at 0000 UTC on 19 July is utilized to verify the improvement of the background. The background field is obtained from the 3 h forecast of the last analysis cycle at 2100 UTC on 18 July. The results are shown in Fig. 5. The comparison clearly shows that the bias and RMSE of experiment ESBM are the smallest among the four experiments, especially for wind components, while only a slight improvement of error reduction can be found in experiment JK. For temperature, the errors from the ESBM experiment are smaller than the others. The bias and RMSE for analysis residual calculated by radiosonde observation minus analysis field (O-A) has also been estimated for CNTL, ESBM and JK, and the conclusions are similar to innovation (figure not shown).

We also compare the distribution of variable differences in initial fields (Fig. 6). At 0000 UTC on 19 July in the T639 global analysis downscaling field, south-central Shaanxi to central Shanxi Province at 700 hPa is the location of a wind shear line (WSL), before which the airflow is southeastern, warm, and moist. At the same time, a deep, dry and cold trough is located behind the WSL. Compared with the GADN experiment, the cold trough of CNTL is relatively weak and the position of the WSL is more northwesterly, from the border between central Shaanxi and Shanxi Provinces to the northwest of Shanxi Province. When examining the difference between the GADN and CNTL experiments (Fig. 6b), we find that the water vapor content of CNTL before the WSL is significantly increased, and the wind fields of the CNTL experiment are stronger than the GADN around the WSLs. For the ESBM experiment (Fig. 6c), the position of WSL and the circulation of the cold trough behind the WSL are similar to GADN, but the water vapor content before the WSL is larger. For experiment JK, the position of the WSL is similar to that in experiment ESBM. It is clear that experiment JK has a similar impact on wind but that humidity is slightly lower than in experiment CNTL (Fig. 6d). For WSL and circulation, there is no significant difference between experiments JK and JKCA.

One important characteristic of composite radar reflectivity at 0000 UTC on 19 July is that the first convection system remained stationary along the eastern foothills of the Taihang Mountains, while the second convection system was located from central Shaanxi Province to central and western Shanxi Province (Fig. 7a). The composite radar reflectivity of experiment CNTL shows that both belt-shaped convection systems are not well captured in the initial field. The first convection system is completely missing, and the second convection system remains along the border of Shanxi

and Shaanxi Provinces, which indicates that the second convection system is eastward moving more slowly than the observation. There are false convections in northwestern Shanxi Province and central and western Henan Province. The result from experiment CNTL shows that after eight 3-hour continuously updated analysis cycles during a 24 h period, the CCDA procedure fails to capture the major characteristics of both convection systems. The composite radar reflectivity of experiment ESBM shows that the first convection system has been captured in the initial field, while the second convection system is located more easterly than the observed location. The composite radar reflectivity of experiment JK is similar to that of experiment CNTL. When considering the three-dimensional cloud analysis, the JKCA experiment is better than in experiment ESBM, and the false convections are restrained. This case shows clearly that for mesoscale analysis, the explicit spatial blending method has a considerable impact on the convection system analysis. Comparing experiments JK and JKCA, we find a benefit is achieved from including radar reflectivity data information. For the mesoscale analysis, the dominant impact comes from mesoscale observations, such as the radar reflectivity used in the cloud analysis. The performances of ESBM and JKCA show that after introducing large-scale and mesoscale observation information into the GRAPES-Meso mesoscale analysis, the initial fields of the convection system are improved.

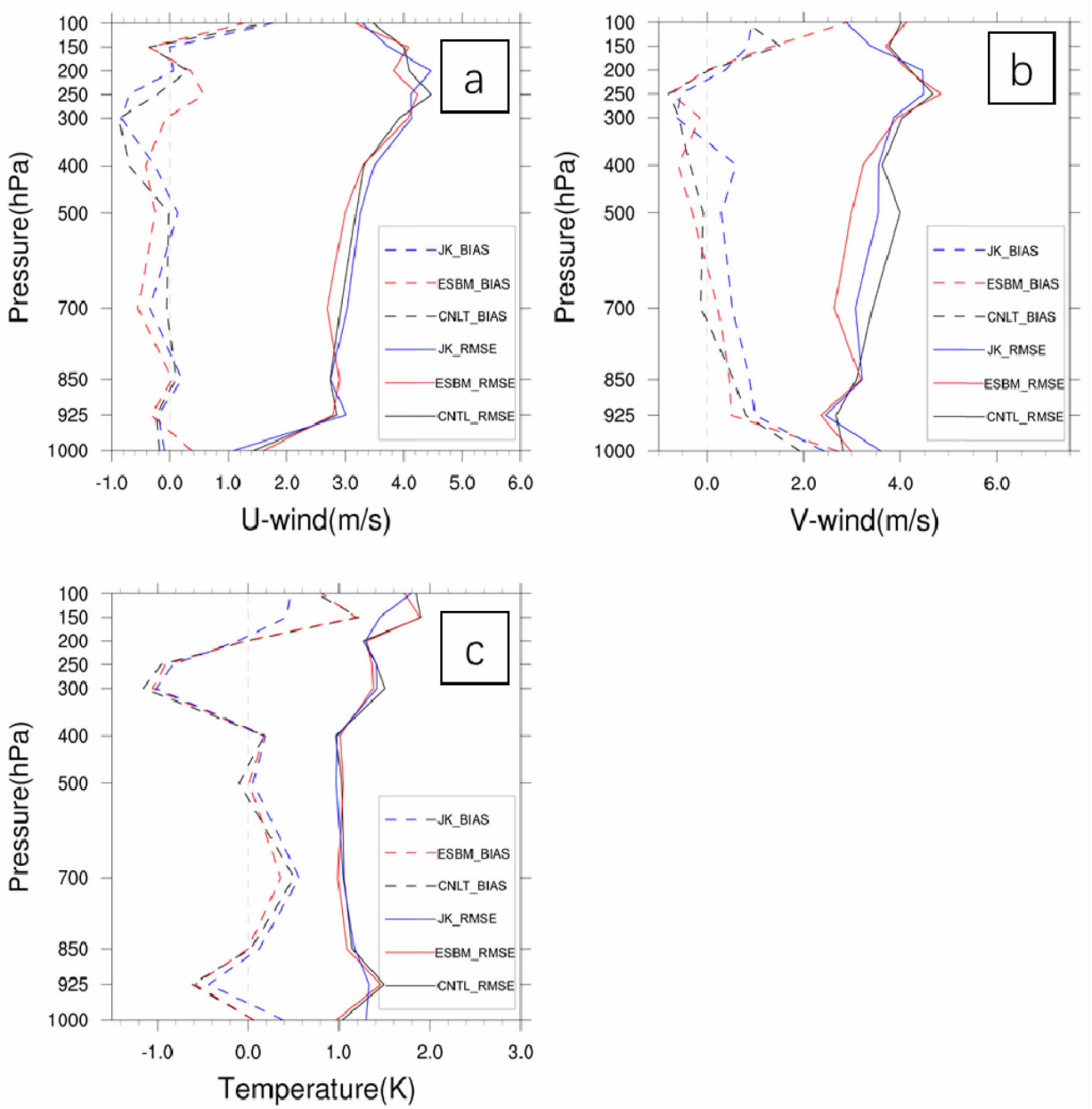

Figure 5. Bias and RMSE of radiosonde innovation. (a) u-wind, (b) v-wind, (c) temperature.

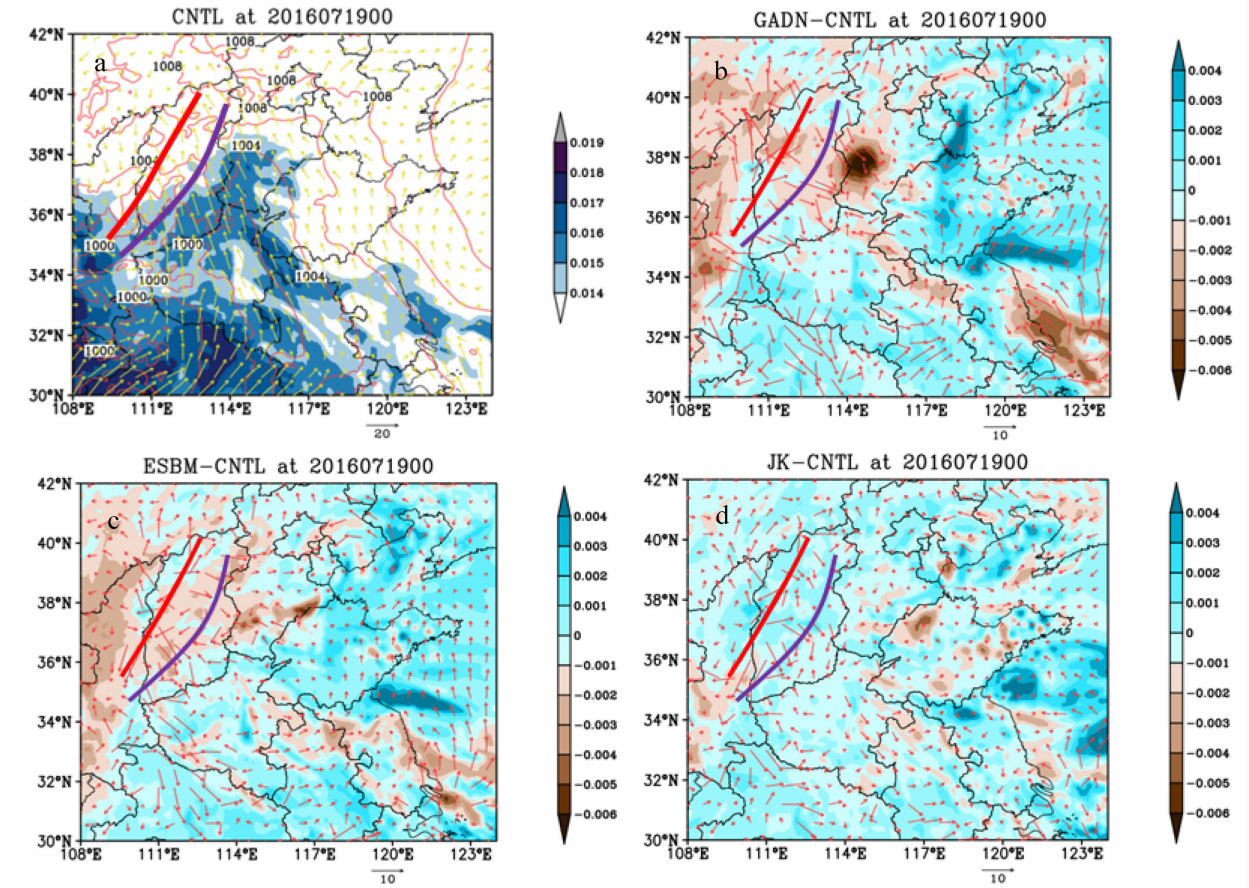

Figure 6. Synoptic charts of the initial field. (a) Initial field of CNTL. The thick red line represents the WSL of experiment CNTL, while the purple line represents experiment GADN. (b) Difference between the initial fields of GADN and CNTL. (c) Difference between ESBM and CNTL. (d) Difference between JK and CNTL. The thick solid line in (a) is the sea-surface pressure isobar (unit: hPa), the arrow is for the wind (unit: m/s), and the shaded area is for specific humidity (unit: kg/kg).

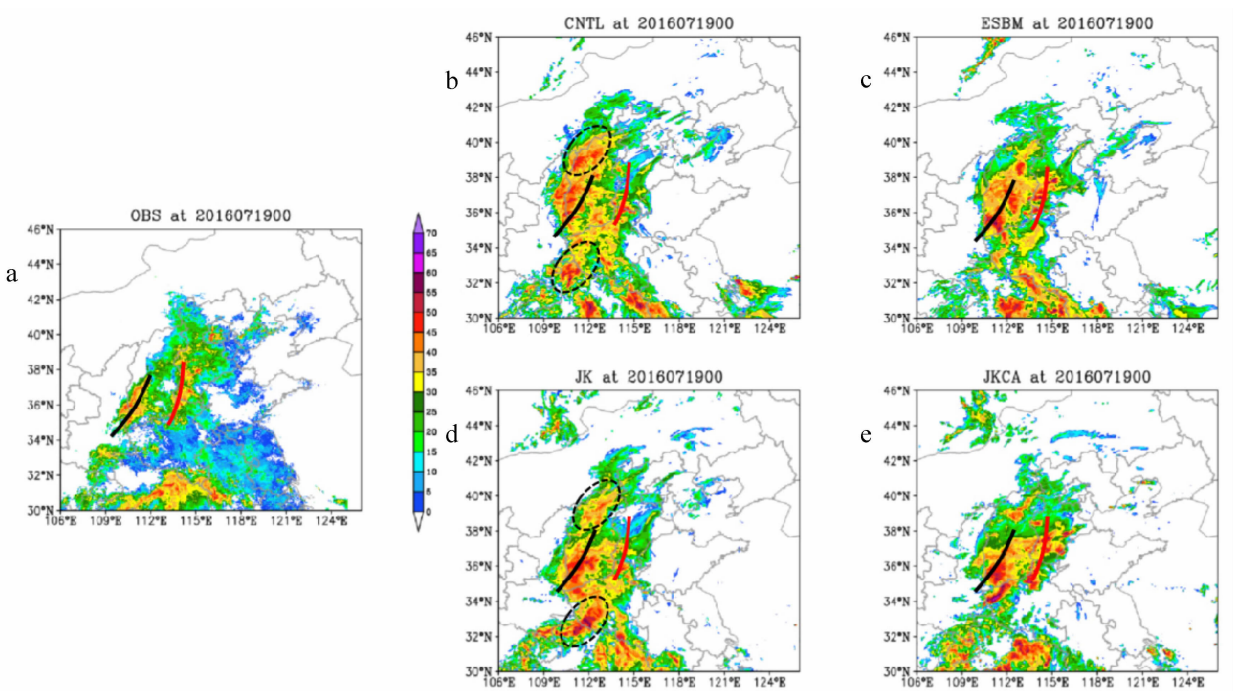

Figure 7. Composite radar reflectivity at 0000 UTC on 19 July. Experiment names are listed in Table 2. (a) Observed composite radar reflectivity. (b)-(e) show the results of experiments CNTL, ESBM, JK and JKCA, respectively. The red line is the position for the first convection system in the radar observation, and the black line is for the second convection system. The dashed circle shows the false composite radar reflectivity.

4.2 *Balance in initial field*

For a rapid update analysis cycle of 3 h or even higher time frequencies, the balance of wind and mass in the initial condition is essential. Vendrasco et al.[17] found that using the 3DVar technique for radar data assimilation could produce spurious precipitation results and large errors in the position and amount of precipitation. One possible reason for the problem is attributed to the lack of proper balance in the dynamical and microphysical fields. In the present study, experiment CNTL may have caused an imbalance between wind and mass in the analysis fields both for the large scale and the convective scale. The explicit spatial blending method utilizes spatial interpolating, transforming, and blending procedures, which will also cause the imbalance problem in the blended analysis field. An investigation of the initial balance properties is desirable and needs to be examined. The domain-averaged absolute surface pressure tendency (ASPT) is calculated to reflect the initial balance properties of model states (Lynch and Huang[11]).

$$N=\frac{1}{I\cdot J}\sum_{i=1}^{I}\sum_{j=1}^{J}\left|\frac{\partial P_S}{\partial t}\right|_{ij} \tag{7}$$

where P_S is the surface pressure and the summation denotes the calculation over the whole GRAPES-Meso model domain.

Figure 8 gives the adjustment of domain average ASPT in every minute over the 1 h forecast. The results show that at first, several model forecast steps in experiments CNTL, ESBM and JK suffer from strong noise, and the value of ASPT is approximately 0.17 hPa/min, which is larger than in experiment GADN. However, the noise dampens very quickly to 0.05 hPa/min, and the pressure tendencies become steady after 10 min. The result of experiment GADN also shows the lack of balance between wind and mass, but the noise is weaker than in the other experiments. The T639 analysis downscaling maintains good balance for the large scale, and it does not contain small-scale information, although those features will be helpful for noise damping. After the first several model forecast steps, the noise in experiment JK is less than in experiment CNTL in the subsequent time, which indicates that considering large-scale information will improve the balance in the mesoscale analysis.

From Fig. 8, when comparing experiments CNTL and ESBM, we find that the two experiments are similar, but experiment ESBM is slightly worse than experiment CNTL. The reason for this difference may be the definition of the transition zone, which is explicitly defined by using a predefined low-pass spatial filter and the same 1,200 km cutoff wavelength for all variables on all model levels, which is not reasonable. Brozkova et al. [10] showed that in the DF blending method, the transition zone is implicitly defined where the spectral coefficients are progressively damped by the digital filter to ensure an appropriate state of balance between the mass and wind initial fields. This process is superior to the explicit procedure used in the present study. It is difficult to provide a reasonable cutoff wavelength for different variables on different model levels with the explicit spatial blending method because the cutoff wavelength is dependent on the day-to-day atmospheric circulation.

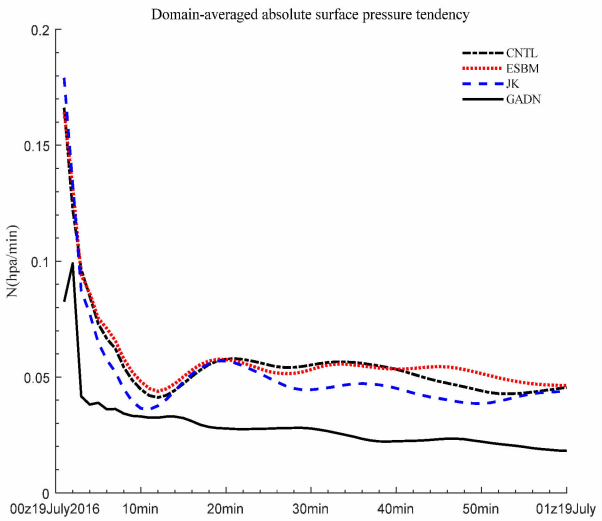

Figure 8. The adjustment of domain-averaged ASPT (unit: hPa/min).

4.3 *RMSE of analysis against ERA data*

To quantitatively evaluate the improvement on a larger scale analysis, we transferred the analyses into the spectral space where waves shorter than 600 km are cut off; thus, only large-scale information is contained in the analyses. Then, the RMSE values for variables u, v, t and q are calculated against the ERA data at 0.5° resolution. The results are shown in Fig. 9. For wind components u and v and temperature T, the RMSEs of experiment CNTL are larger than in the other experiments. According to our discussion in the previous text, experiment CNTL holds improved mesoscale information but with distorted large-scale information due to model bias together with observation bias and the lack of observations over the domain, etc. In contrast, experiment GADN has the smallest error among all of the experiments, which is reasonable because both ERA data and T639 analysis downscaling are global model data and are closer to each other. Compared with GADN, adequate performance of ESBM can only be found in wind component v. It should be noted that the temperature in the GRAPES-Meso analysis is deduced by Exner pressure π and potential temperature θ according to the hydrostatic relationship, which is not conserved for the non-hydrostatic cloud-resolving higher resolution model (Vetra-Carvalho et al.[33]). The performance of JK is less desirable than that in ESBM because the large-scale information in ESBM is directly replaced by the explicit spatial blending method, while experiment JK only uses the weighted constraint

term in the 3DVar cost function to force the analysis field to be closer to global analysis. For specific humidity, the RMSE of experiment JK is the smallest below 700 hPa, and the RMSE profiles of ESBM and GADN are closer.

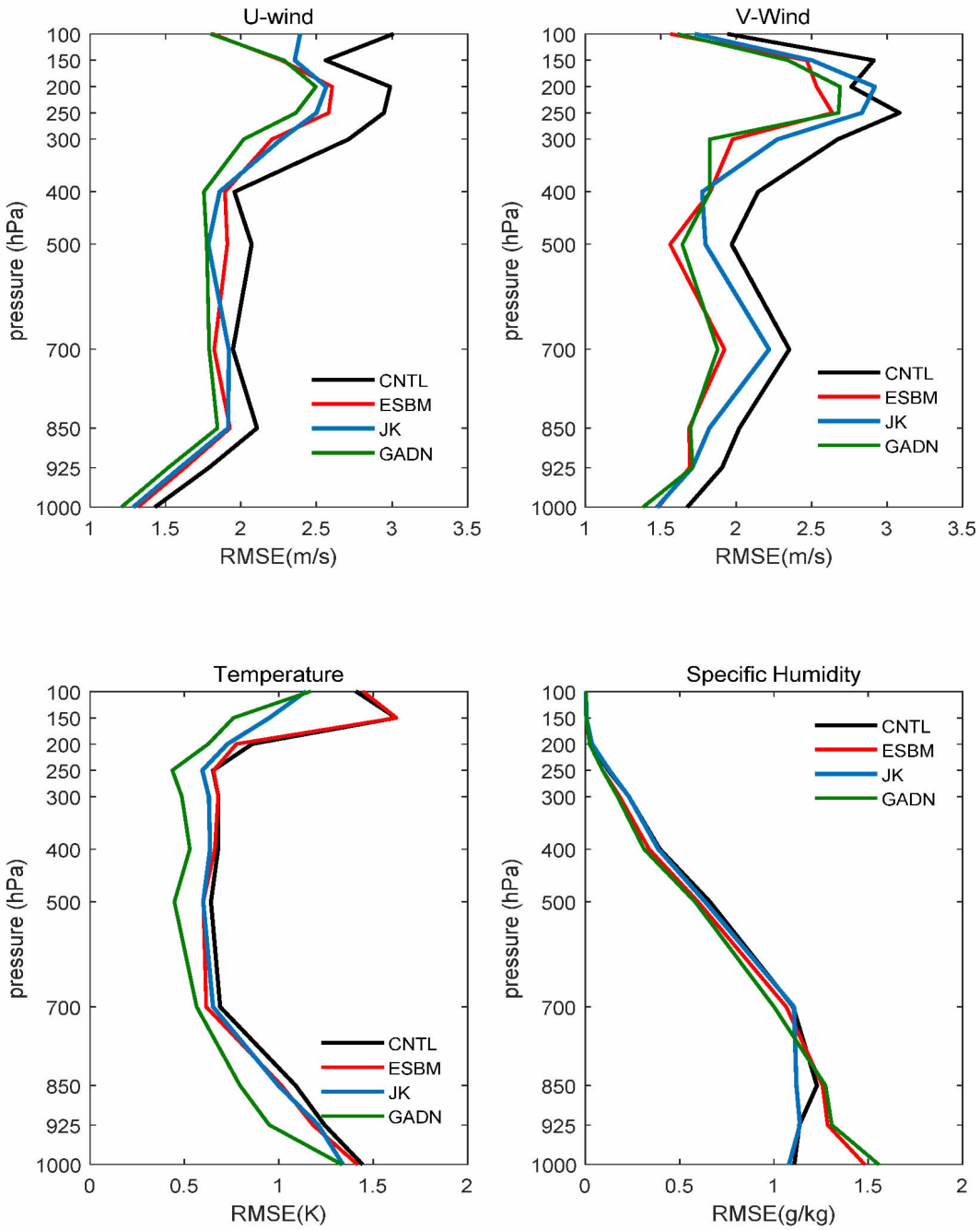

Figure 9. RMSEs for wind (top panels), temperature (left bottom panel), specific humidity (right bottom panel) fields of the experiments against the ERA data at 0.5° resolution.

5 IMPACT ON FORECASTS

5.1 *Composite radar reflectivity and low vortex*

The composite radar reflectivity (CRR) of the forecasts is presented in Fig. 10 to directly compare the forecasts of the mesoscale information. As shown in Fig. 10, the main synoptic characteristic at 0600 UTC on 19 July is the convergence of two convection systems in the eastern foothills of the Taihang Mountains. Obviously, the convergence of two belt-shaped convection systems in CNTL has not occurred yet because the second convection system is still located in the central part of Shanxi Province, far from the fist convection system in the south. The reason for this delay may be explained by the corresponding initial condition at 0000 UTC on 19 July, in which the second convection system also moves more slowly than the observation (Fig. 7). The merging of two convection systems at 0600 UTC on 19 July in the ESBM and JKCA experiments is better than the performance of experiment JK, and all are superior to CNTL.

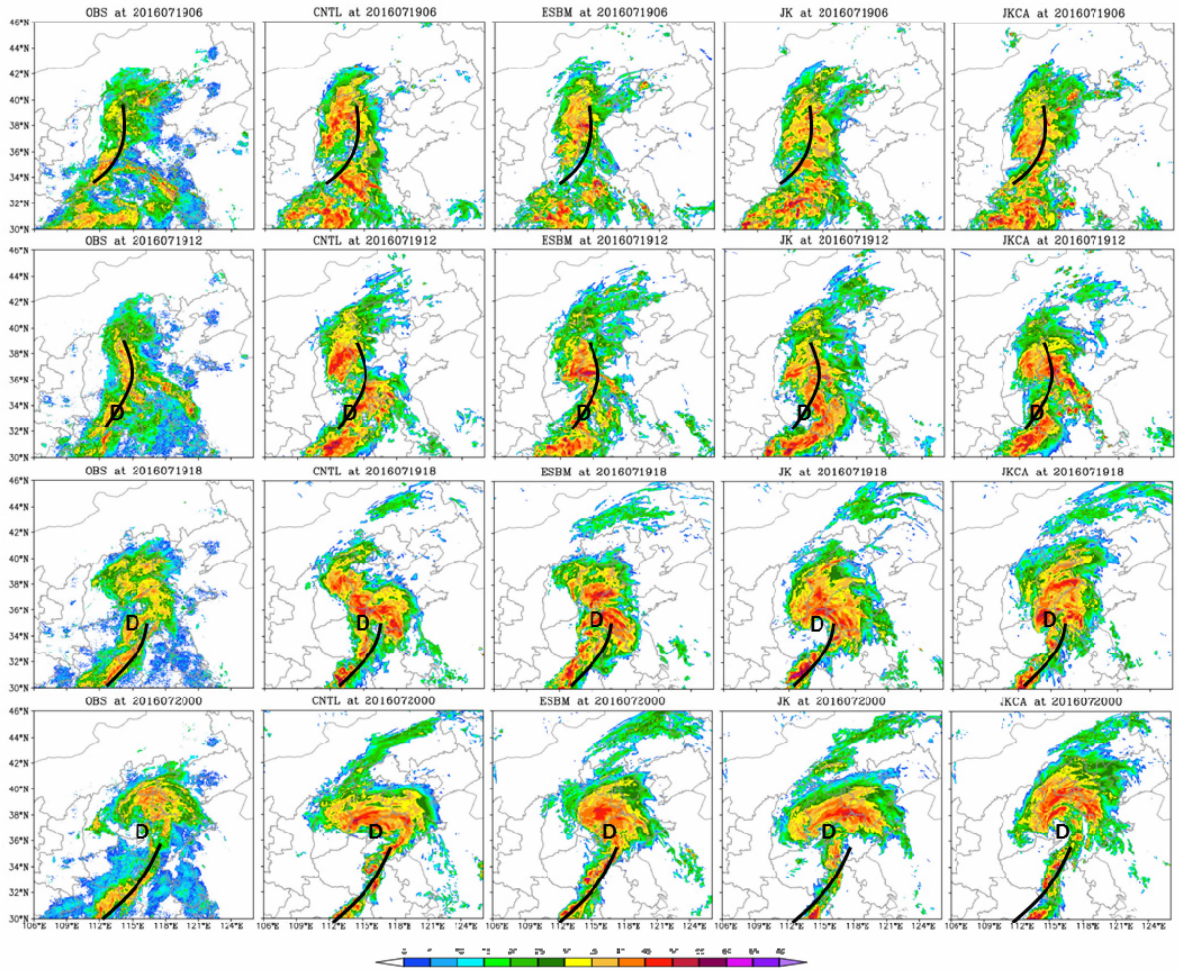

Figure 10. CRR at 0600, 1200, and 1800 UTC on 19 July and 0000 UTC on 20 July. The time increases from top to bottom by 6 h. The first row shows the CRR. Maps on the second row from right to left represent experiments CNTL, ESBM, JK and JKCA, respectively. The black line indicates the observed convection system of interest. "D" indicates the center of the LVCS from the ERA data.

According to the second row of Fig. 10, at 1200 UTC on 19 July, a newborn cyclone in the observation remains stationary along the eastern foothills of the Taihang Mountains. Compared with the observation, the performance of CNTL is less desirable than that of ESBM and JKCA. At the same time, an LVCS has formed in the central part of Henan Province. Fig. 11 shows the low vortex's track calculated by the sea-surface pressure minimum and 85 hPa vorticity. According to Figs. 10 and 11, the four experiments, i.e., CNTL, ESBM, JK and JKCA, capture the generation of this structure but with different locations. Compared with the ERA data, the positions of LVCS in experiments CNTL and JKCA are located eastward, while in ESBM, they are more southeastward. In summary, experiments JK and JKCA generate more reasonable vortex circulation structures than the other experiments.

At 1800 UTC on 19 July (third row of Fig. 10), the LVCS develops and moves northeastward slowly, and the position of low vortex is mainly in the northern part of Henan Province. At 0000 UTC on 20 July, this mature cyclone moves slowly northward and reaches the

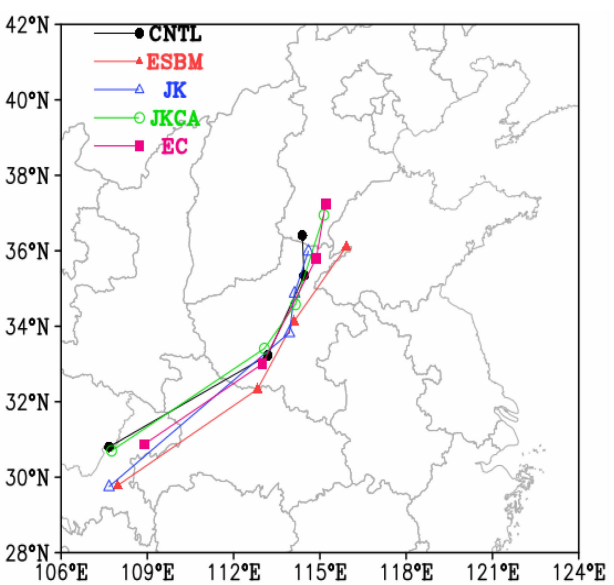

Figure 11. The LVCS path prediction at 0000 UTC on 19 to 20 July. The position of the LVCS is calculated by the sea-surface pressure minimum and 850 hPa vorticity. EC represents the ECMWF ERA data.

southern part of Hebei Province, bringing about heavy precipitation mainly centered in two regions. The first location of heavy precipitation is in the south of the cyclone and near the cold front, and the second location is in the north of cyclone and near the strong wind shear. For the first region, experiments CNTL, ESBM and JKCA could capture the cold front in the southern vortex. For the second region, the location forecast of CNTL is more southward than the observation. The observed maximum CRR lies in southern Beijing. In contrast, however, the maximum CRR of experiment CNTL lies in southern Hebei Province and northwestern Shandong Province. Experiment ESBM is similar to experiment CNTL, but JK and JKCA are both correct in forecasting the position of the maximum CRR. From the track forecast of the vortex (Fig. 10), we can conclude that the track predictions of experiments JK, JKCA and CNTL are closer to the ERA data; however, the performance of ESBM is not satisfactory.

5.2 *RMSE of the forecast field*

To quantitatively evaluate the improvement of forecasts, the RMSEs for the wind component, temperature and specific humidity fields of the four experiments against the ERA data at 0.5° resolution are calculated. The RMSE profiles of the 12 h forecast (at 1200 UTC on 19 July) are shown in Fig. 12. For wind components u and v, the RMSE of experiment CNTL is the largest, and significant improvement can be found in experiment ESBM, while the RMSE reduction for experiments JK and JKCA is only slight, especially for the wind components in lower levels at approximately 500 to 1,000 hPa. For temperature, only the RMSE of experiment ESBM has a visible improvement between levels 400 and 850 hPa, and the performances of JK and JKCA are relatively neutral. For specific humidity, we also find that experiment ESBM has the smallest RMSE distributions except for levels below 850 hPa, and the forecast accuracy of experiments JK and JKCA is only

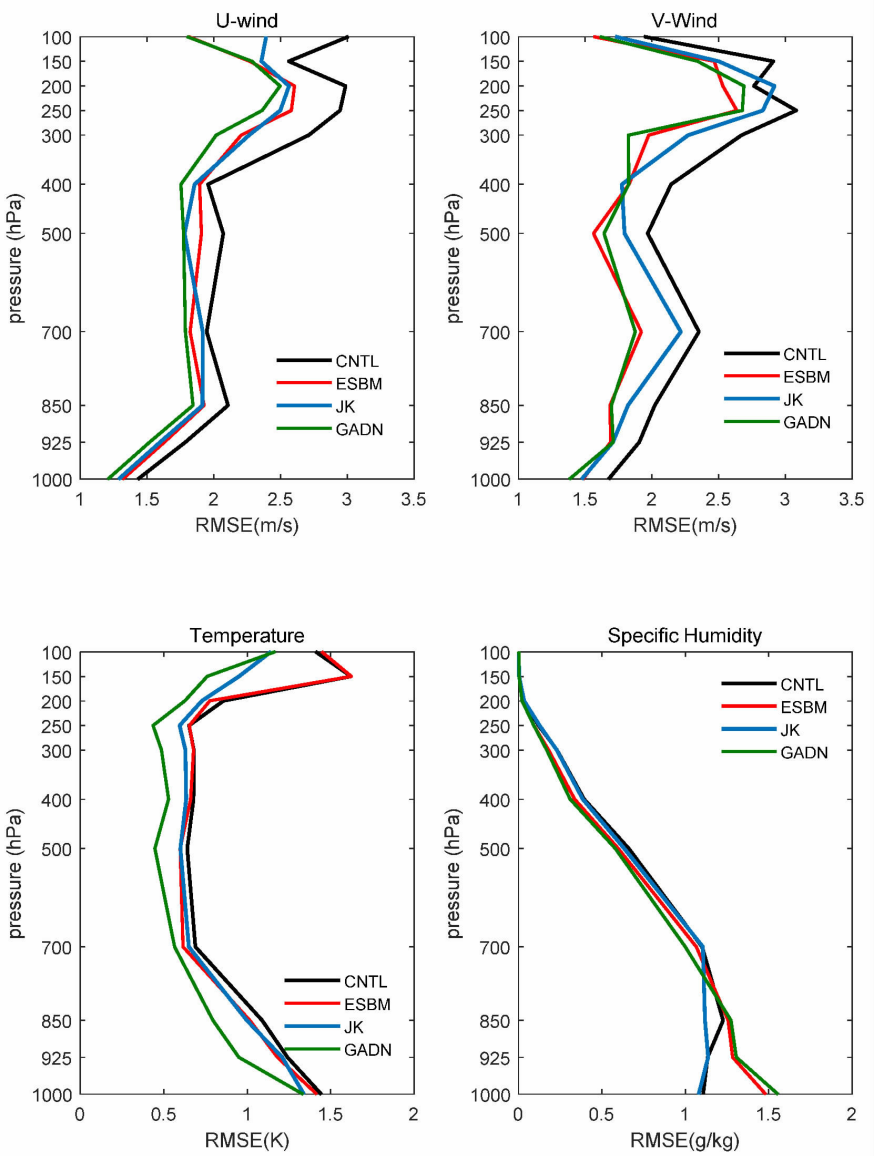

Figure 12. The RMSE of the forecast field at 1200 UTC on 19 July for wind (top panels), temperature (left bottom panel) and specific humidity (right bottom panel) fields of experiment against the ERA data at 0.5° resolution.

slightly improved. The RMSE profiles of the 24 h forecasts (figure not shown) are also calculated, and the conclusions are generally similar to those of the 12 h forecasts.

5.3 *Precipitation forecast*

The horizontal distributions of the 24 h accumulative precipitation forecasts during 0000 UTC on 19-20 July of the four experiments are given in Fig. 13. As shown in Fig. 2, most of the heavy precipitation over 50 mm/d is centered in southern Beijing, Hebei Province, and the central part of Hubei Province and on the border between Chongqing and Hunan Province. According to Fig. 13, experiments CNTL, ESBM and JK fail to forecast the heavy precipitation that occurred in southern Beijing, and only experiment JKCA is accurate regarding the location, but the intensity predicted is clearly not heavy enough. Additionally, considerable spurious heavy precipitation is forecasted in experiment CNTL in eastern Shanxi Province, which is corrected in experiment ESBM but still exists in both the JK and JKCA experiments. CNTL failed to capture the precipitation near the border between Chongqing and Hunan Province, while the other three experiments are slightly closer to the target. In summary, the horizontal pattern of accumulative precipitation of experiment JKCA is most similar to the observation.

From 0000 UTC on 19 to 20 July, heavy and persistent precipitation caused by a new belt-shaped convection system was located from Shijiazhuang, Hebei Province, to Anyang, Henan Province. The observed accumulative rainfall was greater than 500 mm and was mainly centered on the belt of this new belt-shaped convection system. The characteristic of orographically forced precipitation is evident. First, the precipitation data between 35.5° N and 38.5° N are averaged to assess the impact (Fig. 14a). The maximum value of the precipitation forecast of experiment JKCA is approximately 150 mm along the eastern foothills of the Taihang Mountains. The precipitation forecast of experiment CNTL has the maximum value of approximately 140 mm along the eastern foothills of the Taihang Mountains, and this value is less than that in experiment JKCA. Fig. 14 (b) also gives an example of accumulated precipitation along 37.75° N, where experiments CNTL, ESBM and JK have greater precipitation in the eastern foothills of the Taihang Mountains. Experiment CNTL reserves the well-featured mesoscale information, leading to an improvement in the precipitation forecast. For experiment ESBM, the precipitation result is similar to that in experiment JK. We also found that the precipitation value over the plant

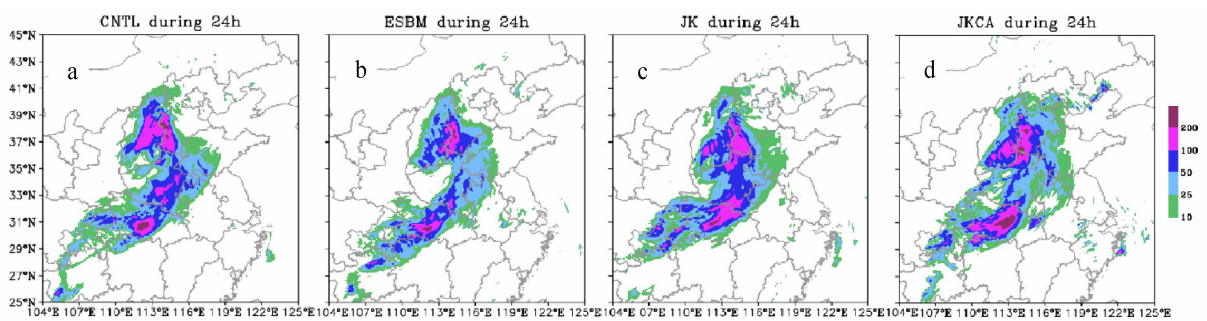

Figure 13. Horizontal pattern of 24 h accumulative precipitation forecast during 0000 UTC on 19-20 July for (a) experiment CNTL, (b) experiment ESBM, (c) experiment JK, and (d) experiment JKCA. The color bar shows the different precipitation thresholds (unit: mm).

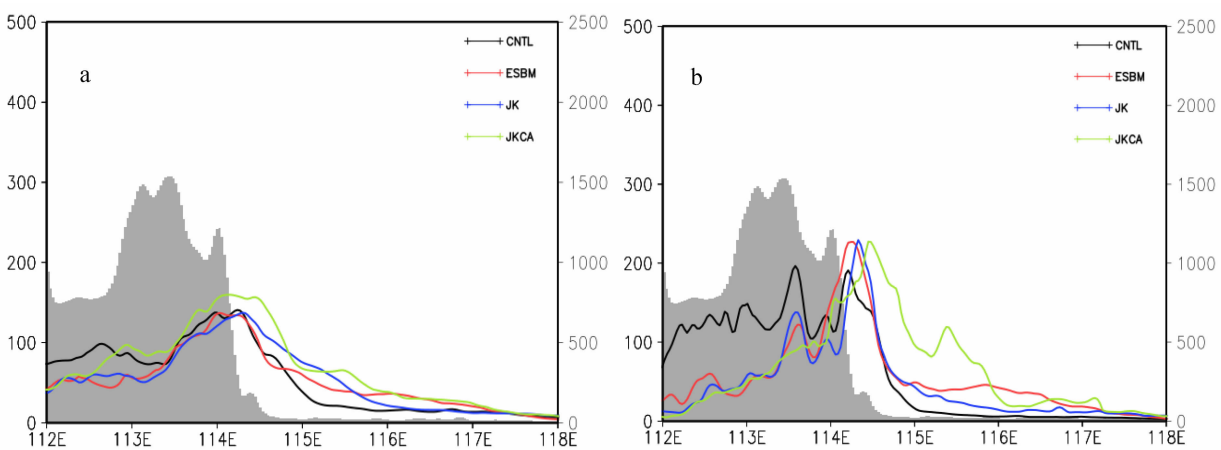

Figure 14. The precipitation forecast in the foothills of the Taihang Mountains; the shaded area is the topography. (a) Precipitation data average between 35.5°N and 38.5°N. (b) Precipitation data along 37.75°N. The left axis is for accumulated precipitation (unit: mm), while the right axis is for topographic height (unit: meters).

region is also increasing. The position of the LV of experiment ESBM is located more southeastward than in the other experiments, which will increase rainfall over the plant region. The precipitation forecast of experiment JKCA is similar to that of experiment CNTL but with more rainfall over the plant region.

5.4 *Precipitation forecast verification*

Two QPF statistics scores, i.e., the equitable threat score (ETS) and frequency bias (BIAS) score, have been calculated to examine the impact of merging large-scale information with mesoscale analysis on precipitation forecasts, which are shown with different thresholds for 24 h forecasts in Fig. 15. The ETS score is defined as follows (Shuman[34]):

$$\mathrm{ETS}=\frac{H-FO/N}{F+O-H-FO/N} \tag{8}$$

Here, F is the forecast area, H is the correctly forecasted area ("hits"), O is the observed area, and N denotes the total number of verification points or events. FO/N is the hits expected from a random forecast. The ETS score measures the fraction of observed and/or forecast events that are correctly predicted, adjusted for correct predictions due to random chance. The bias score is defined as follows (Mcbride and Ebert[35]):

$$\mathrm{BIAS}=\frac{FA+H}{M+H} \tag{9}$$

Here, FA is the false alarm area and M is the missing area. The bias score is equal to the area of rain forecasts divided by the total area of observations of rain. Thus, the bias score measures the relative frequency of rain forecasts compared with observations. Larger ETS values indicate higher QPF accuracy while BIAS values above (below) 1 imply an overestimate (underestimate).

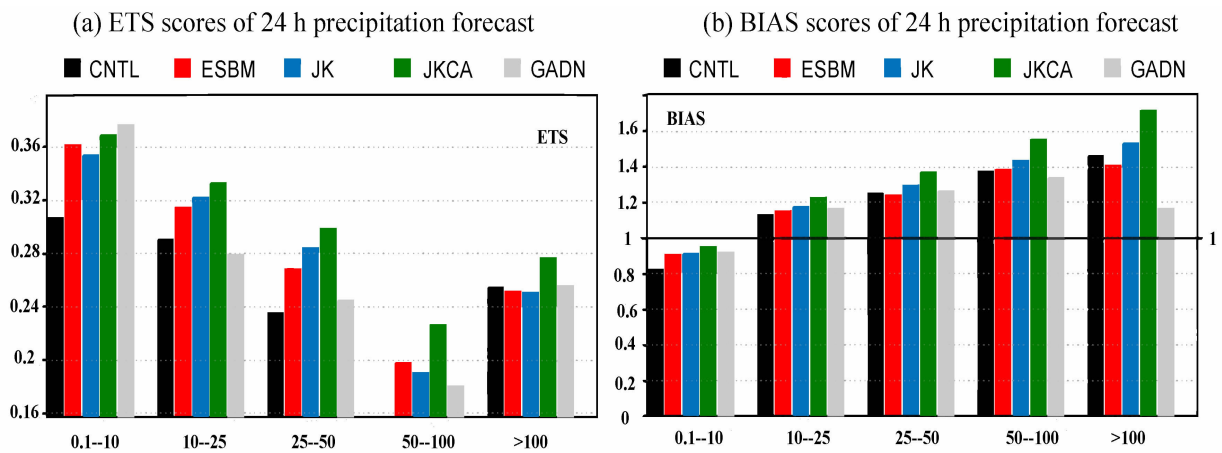

Figure 15. ETS and BIAS scores for the 24 h precipitation forecast. (a) ETS score; (b) BIAS core. The precipitation threshold score of 0.1-10 mm/d (light precipitation), 10-25 mm/d (moderate precipitation), 25-50 mm/d (large precipitation), 50-100 mm/d (heavy precipitation), greater than 100 mm/d (severe heavy precipitation) are shown in the color bar.

The verification is against the dataset from 24 h of cumulative precipitation in 2,500 rain gauge stations over China. Compared to the T639 analysis downscaling forecast, the CNTL experiment has a poor ETS score for a light precipitation threshold of 0.1 mm/d, and the performance of the BIAS score is also less than that of GADN. The undesirable ETS and BIAS light precipitation scores mean that the CNTL precipitation forecast pattern is significantly different from the observations. The ETS score of the CNTL experiment forecast is better than that of the GADN experiment for a moderate precipitation threshold of 10 mm/d. Moderate precipitation is generally caused by persistent precipitation. The GADN and CNTL experiments have clearly shown the characteristics of both global analysis downscaling and mesoscale analysis from continuously cycled analysis. Experiment GADN provides useful large-scale information but with a poor description of mesoscale information. In contrast, experiment CNTL provides improved mesoscale information but with distorted large-scale information.

For experiment ESBM with a cutoff wavelength of 1,200 km, the ETS score for light precipitation is dramatically improved compared with that of experiment CNTL and is closer to that of experiment GADN. For moderate precipitation and large precipitation, the ESBM experiment forecasts are far superior to those of experiments GADN and CNTL. This superiority could also be found for the heavy precipitation threshold of 50 mm/d. The heavy precipitation is generally caused by severe convective systems whose spatial scales are smaller. From the precipitation verification score, we find that the explicit spatial blending method could take advantage of both large-scale information from global analysis and mesoscale information from CCDA. The JK experiment has a similar performance to experiment ESBM for the light precipitation ETS score but has a clear benefit for moderate and large precipitation ETS scores. The BIAS scores of experiment JK are slightly larger than those of experiment ESBM, which means that precipitation is slightly overestimated. This benefit of experiment JK may come from a well-balanced

small-scale structure in the initial condition in the constraining method, as displayed and discussed in the last section. According to the three-dimensional cloud analysis, it is clear that for almost all precipitation thresholds, experiment JKCA is better than experiment JK and experiment ESBM. The dominant information in the cloud analysis comes from radar reflectivity. This result is not surprising and again confirms that merging both the large-scale and mesoscale information will improve the precipitation forecast. For cloud-resolving model resolution and a small domain with a few observations, the constraining method is better than the blending method in this case study.

6 CONCLUSIONS

GRAPES-Meso 4.0 suffers from the weakness of large model bias, deficiency of locally dense observation data, and the absence of satellite radiance data, which can be quite important over the ocean. To reduce the error of the GRAPES-Meso analysis, we adopt the blending method from Yang[13] and the constraining method from Guidard and Fischer[8] to merge the large-scale analysis information from the T639 global model with the mesoscale analysis data from GRAPES-Meso 3Dvar. Both methods are utilized in GRAPES-Meso CCDA. An extremely severe precipitation event in northern China on 19-20 July 2016 is selected for study in this paper. The 24 h period CCDA with a 3 h updated analysis cycle is used to obtain the initial condition, after which a 24 h forecast is performed. Comparative studies of the blending and constraining method are performed to find a suitable method for GRAPES-Meso CCDA.

In experiment ESBM, larger-scale information in the initial field is directly replaced by T639 large-scale information through the explicit spatial blending method, while experiment JK only uses the weighted constraint term in the cost function of 3DVar to force the analysis field to be closer to the global larger-scale information. The initial fields are cut off at the 600 km wavelength to represent large-scale information and compared with ERA data at 0.5 resolution. The wind components of experiment JK are slightly worse than those of experiment ESBM, but they are all better than those of experiment CNTL. For temperature and specific humidity, the result is neutral. At the same time, the convection systems in the initial field are also improved, especially for experiment ESBM, while experiment JK shows slight improvement. Comparing the 3 h background with the radiosonde observation shows that after introducing large-scale information, the background is slightly closer to the radiosonde observations, and experiment ESBM is better than experiment JK. This means that blending and constraining T639 large-scale information into the GRAPES mesoscale analysis is superior to not using that information. Because the constraining method is based on 3DVar to merge large-scale information, the balance between wind and mass is better than that of explicit spatial blending; the latter utilizes spatial interpolating, transforming, and blending procedures, which will cause an imbalance problem in the blended analysis field.

In this study, the weakness of the constraining method is mainly focused on the assumption that the large-scale analysis error covariance matrix for wind, temperature, and humidity is an uncorrelated diagonal matrix. Dahlgren and Gustafsson[16] used the same approach but only assimilated the vorticity field from the global analysis with global analysis error covariances that are not simplified by a diagonal matrix, as in Guidard and Fischer[8]. This study provides preliminary research on improving the analysis error covariance. The large-scale error covariance matrix still needs to be enhanced to better represent large-scale analysis information introduced in mesoscale analysis. The simplification of the large-scale analysis error covariance matrix in this study is one of the major reasons why experiment JK is not as effective as ESBM in the analysis verification. Meanwhile, accurately providing large-scale analysis error variance is important for experiment JK.

For the forecast performance, the impact of the blending and constraining method is significant at first for the 12 h forecast period for convection systems. The evolution of the belt-shaped convection system is described better by experiment ESBM than by experiment JK. Experiment CNTL is worse than experiments ESBM and JK. When focused on the full model domain, the 24 h precipitation forecast verified by ETS score and BIAS score clearly shows that experiment JK is better than experiment ESBM. When comparing experiment JKCA and the other experiments, the results show that for the mesoscale analysis, the dominant impact came from the mesoscale observation information, such as the radar reflectivity data used in the cloud analysis, which will influence the forecast. Overall, the 24 h precipitation forecast of experiment JKCA is the best among all the experiments.

It is important to note that almost equally good performance could be found in both methods, but the blending method is more effective in introducing the large-scale analysis. In our study, either the analysis or forecast derived by the blending or constraining method indeed offers better performance than the original GRAPES-Meso or T639 methods. Moreover, the technical realization of explicit spatial blending is more complicated and tedious, and the variety of the cutoff wavelengths on different variables and different model levels are not taken into account. Additionally, the computation cost is only slightly increased in the constraining method.

It should be noted that the research findings in this paper are mainly based on a case study, and certain randomness is inevitable. Therefore, a series of batch experiments to sufficiently verify the results will be included in the future work. Nevertheless, the analysis

and forecasts are effectively improved in this study, which provides a reference for subsequent improvement of the GRAPES-Meso analysis.

Acknowledgement: We gratefully acknowledge Dr. DENG Lian-tang for guidance in using the verification tools. Special thanks go to Dr. HUANG Li-ping, Dr. ZHANG Li-hong, Dr. LI Shao-ying, and Dr. XIA Yu for their support and discussion.

REFERENCES:

[1] BERRE L. Estimation of synoptic and mesoscale forecast error covariances in a limited area model [J]. Mon Wea Rev, 2000, 128(3): 644-667.

[2] HSIAO L F, LIOU C S, YEH T C, et al. A vortex relocation scheme for tropical cyclone initialization in Advanced Research WRF [J]. Mon Wea Rev, 2010, 138 (8): 3298-3315.

[3] ROMINE G S, SCHWARTZ C S, SNYDER C, et al. Model bias in a continuously cycled assimilation system and Its influence on convection-permitting forecasts [J]. Mon Wea Rev, 2013, 141(4): 1263-1284.

[4] SIROKA M, BOLONI G, BROZKOVA R, et al. Innovative developments for a 3DVar analysis in a limited area model: Scale selection and blended cycling[R]. WMO CAS/JSC WGNE Report 31, 2003, 1.53-1.54.

[5] ZHANG Cheng-zhong, CHEN Zi-tong, WAN Qi-lin. Application experiment of assimilating radar-retrieved water vapor in short-range forecast of rainfall in the annually first season over south China [J]. J Trop Meteor, 2016, 32(4): 578-588 (in Chinese).

[6] BERRE L, STEFANESCU S E, PEREIRA M B. The representation of the analysis effect in three error simulation techniques [J]. Tellus A, 2006, 58(2): 196-209.

[7] DAVIES H. A lateral boundary formulation for multi-level prediction models [J]. Quart J Roy Meteor Soc, 1976, 102 (432): 405-418.

[8] GUIDARD V, FISCHER C. Introducing the coupling information in a limited area variational assimilation [J]. Quart J Roy Meteor Soc, 2008, 134(632): 723-736.

[9] SADIKI W, FISCHER C, GELEYN J F. Mesoscale background error covariances: Recent results obtained with the limited area model ALADIN over Morocco[J]. Mon Wea Rev, 2000, 128(11): 3927-3935.

[10] BROZKOVA R, KLARIC D, IVATEK-SAHDAN S, et al. DFI blending, an alternative tool for preparation of the initial conditions for LAM [R]. PWRP Report Series No. 31, WMO-TD, No. 1064, 2001.

[11] LYNCH P, HUANG X Y. Initialization of the HIRLAM model using a digital filter [J]. Mon Wea Rev, 1992, 120 (6): 1019-1034.

[12] GUIDARD V, FISCHER C, NURET M, et al. Evaluation of the ALADIN 3D-Var with observations of the MAP campaign [J]. Meteor Atmos Phys, 2006, 92 (3-4): 161-0173.

[13] YANG X. Analysis blending using a spatial filter in grid-point model coupling[J]. HIRLAM Newsletter, 2005, 48: 49-55.

[14] WANG H, HUANG X Y, XU D, et al. A scale-dependent blending scheme for WRFDA: Impact on regional weather forecasting[J]. Geosci Model Dev, 2014, 7(2), 7: 1819-1828.

[15] HSIAO L F, HUANG X Y, KUO Y H, et al. Blending of global and regional analyses with a spatial filter: application to typhoon prediction over the Western North Pacific Ocean [J]. Wea Forecasting, 2017, 30(3): 754-770.

[16] DAHLGREN P, GUSTAFSSON N. Assimilating host model information into a limited area model[J]. Tellus A, 2012, 64(1): 1-19, doi: 10.3402/tellusa.v64i0.15836.

[17] VENDRASCO E P, SUN J, HERDIES D L, et al. Constraining a 3DVAR radar data assimilation system with large-scale analysis to improve short-range precipitation forecasts [J]. J Appl Meteor Climatol, 2016, 55(3): 673-690.

[18] HUANG L P, CHEN D H, DENG L T, et al. Main technical improvements of GRAPES-Meso 4.0 and verification[J]. J Appl Meteor Sci, 2017, 28(1): 25-37 (in Chinese).

[19] WANG Jing, XU Zhi-fang, FAN Guang-zhou, et al. Study on bias correction for the 2m temperature forecast of GRAPES_RAFS [J]. Meteor Mon, 2015, 41(6): 719-726 (in Chinese).

[20] XU Chen-lu, WANG Jian-jie, HUANG Li-ping. Evaluation on QPF of GRAPES-Meso4.0 model at convection-permitting resolution [J]. Acta Meteor Sinica, 2017, 75(6): 851-876 (in Chinese).

[21] RAYMOND W H, GARDER A. A review of recursive and implicit filters[J]. Mon Wea Rev, 1991, 119(2): 477-495.

[22] ZHANG Han-bin, CHEN Jing, ZHI Xie-fei, et al. Study on multi-scale blending initial condition perturbations for a regional ensemble prediction system [J]. Adv Atmos Sci, 2015, 32(8): 1143-1155.

[23] DENIS B, COTE J, LAPRISE R. Spectral decomposition of two-dimensional atmospheric fields on limited-area domains using the discrete cosine transform (DCT) [J]. Mon Wea Rev, 2002, 130(7): 1812-1829.

[24] ZHENG Yong-jun, JIN Zhi-yan, CHEN De-hui. Kinetic energy spectrum analysis in a semi-implicit semi-Lagrangian dynamical framework[J]. Acta Meteor Sinica, 2008, 66(2): 143-157 (in Chinese).

[25] DERBER J, BOUTTIER F. A reformulation of the background error covariance in the ECMWF global data assimilation system [J]. Tellus A, 1999, 51A: 195-221.

[26] PARRISH D F, DERBER J C. The National Meteorological Center's spectral statistical-interpolation analysis system [J]. Mon Wea Rev, 1992, 120 (8): 1747-1763.

[27] SAVIJARVI H. Error growth in a large numerical forecast system [J]. Mon Wea Rev, 1995, 123(1): 212-221.

[28] FU Jiao-lan, MA Xue-kuan, CHEN Tao, et al. Characteristics and synoptic mechanism of the July 2016 extreme precipitation event in north China[J]. Meteor Mon, 2017, 43(5): 528-539(in Chinese).

[29] MA Xu-lin, ZHUANG Zhao-rong, XUE Ji-shan, et al. Developments of the three-dimensional variational data assimilation system for the nonhydrostatic GRAPES [J]. Acta Meteor Sinica, 2009, 23(3): 725-737 (in Chinese).

[30] ZHANG Xu-bin, XUE Ji-shan, WAN Qi-lin, et al. Study on time-dependent and multi-scale background error covariance I: Construction[J]. J Trop Meteor, 2014, 30 (4): 675-686 (in Chinese).

[31] ZHANG Xu-bin, XUE Ji-shan, WAN Qi-lin, et al. Study on time-dependent and multi-scale background error

covariance II: Application[J]. J Trop Meteor, 2015, 31(2): 161-172 (in Chinese).

[32] ZHU Li-juan, GONG Jian-dong, HUANG Li-ping, et al. Three dimensional cloud initial field created and applied to GRAPES numerical weather prediction nowcasting. [J]. J Appl Meteor Sci, 2017, 28(1): 38-51 (in Chinese).

[33] VETRA-CARVALHO S, DIXON M, MIGLIORINI S, et al. Breakdown of hydrostatic balance at convective scales in the forecast errors in the Met Office Unified Model[J]. Quart J Roy Meteor Soc, 2012, 138(668): 1709-1720.

[34] SHUMAN F G. A modified threat score and a measure of placement error [R]. NOAA/NWS Office Note 210, 13 pp., available at: http://wwwt.emc.ncep.noaa.gov/officenotes, 1980.

[35] McBRIDE J L, EBERT E. Verification of quantitative precipitation forecasts from operational numerical weather prediction models over Australia[J]. Wea Forecasting, 2000, 15(1): 103-121.

Citation: YANG Mei-jin, GONG Jian-dong, WANG Rui-chun, et al. A comparison of the blending and constraining methods to introduce large-scale information into GRAPES mesoscale analysis [J]. J Trop Meteor, 2019, 25(2): 227-244.